

Digital control of force microscope cantilevers using a field programmable gate array

Jonathan P. Jacky,^{1,*} Joseph L. Garbini,² Matthew Ettus,³ and John A. Sidles¹

¹*Department of Orthopaedics and Sports Medicine, University of Washington*

²*Department of Mechanical Engineering, University of Washington*

³*Ettus Research LLC*

Abstract

This report describes a cantilever controller for magnetic resonance force microscopy (MRFM) based on a field programmable gate array (FPGA), along with the hardware and software used to integrate the controller into an experiment. The controller is assembled from a low-cost commercially available software defined radio (SDR) device and libraries of open-source software. The controller includes a digital filter comprising two cascaded second-order sections ("biquads"), which together can implement transfer functions for optimal cantilever controllers. An appendix in this report shows how to calculate filter coefficients for an optimal controller from measured cantilever characteristics. The controller also includes an input multiplexer and adder used in calibration protocols. Filter coefficients and multiplexer settings can be set and adjusted by control software while an experiment is running. The input is sampled at 64 MHz; the sampling frequency in the filters can be divided down under software control to achieve a good match with filter characteristics. Data reported here were sampled at 500 kHz, chosen for acoustic cantilevers with resonant frequencies near 8 kHz. Inputs are digitized with 12 bits resolution, outputs with 14 bits. The experiment software is organized as a client and server to make it easy to adapt the controller to different experiments. The server encapsulates the details of controller hardware organization, connection technology, filter architecture, and number representation. The same server could be used in any experiment, while a different client encodes the particulars of each experiment.

arXiv:0809.1403v1 [physics.ins-det] 8 Sep 2008

*Electronic address: jon@u.washington.edu; Mailing address: University of Washington, Mechanical Engineering, Box 352600, Seattle, Washington, 98195-2600

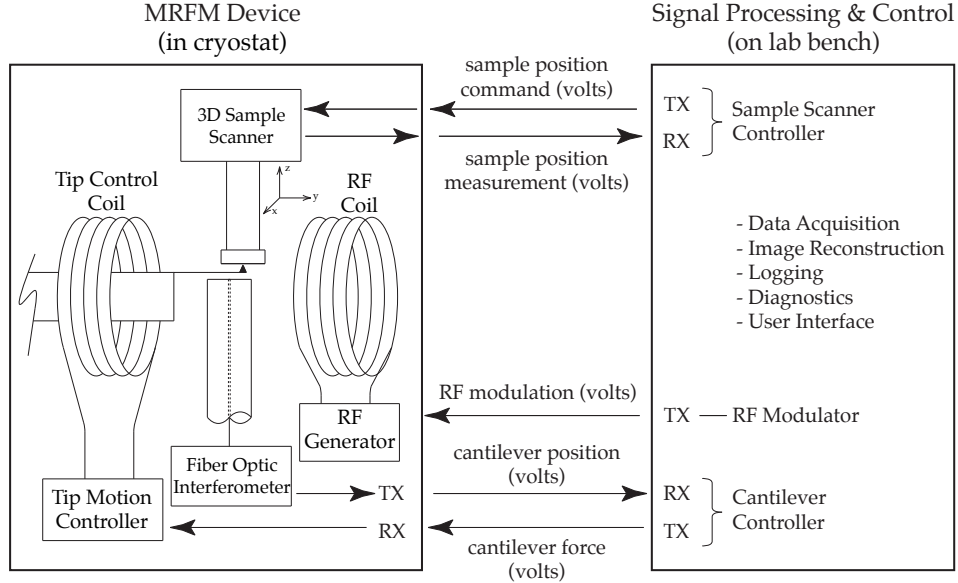


FIG. 1: MRFM experiment

I. INTRODUCTION

This report describes a cantilever controller for magnetic resonance force microscopy (MRFM) based on a field programmable gate array (FPGA). The controller is assembled from a low-cost commercially available software defined radio (SDR) device, libraries of open-source software, and some additional software that we have written. In addition to the controller itself, we also describe software that integrates the controller into an experiment. We show how to calculate filter coefficients for an optimal controller from measured cantilever characteristics. Finally, we present data comparing calculated and measured controller performance.

Force microscope cantilevers are mechanical oscillators that require feedback control. In MRFM, cantilevers sense the magnetic force exerted by spins in the sample [1, 2]. Cantilevers for detecting such small forces must have low spring constants and high quality factors, but these result in large deflections, long ring-down times, and narrow bandwidth, which hinder image acquisition. These effects can be mitigated by feedback control without affecting the signal-to-noise ratio for force measurement [3]. In the apparatus shown in Fig. 1, the cantilever controller would be connected between RX and TX in the lower right corner (RX is the controller input).

Cantilever controller design is discussed in [3, 4, 5, 6]; details of our design appear in the appendix. Early controllers used analog circuits including operational amplifiers [4, 5]; recent controllers use specialized microprocessors called Digital Signal Processors (DSPs) [6, 7]. In this report we describe a new digital cantilever controller based on an FPGA.

An FPGA contains an array of identical digital logic and memory elements which can be connected together under software control to form, in effect, a custom integrated circuit. FPGA-based signal processors can have several advantages over microprocessors (including DSPs). Computations can be highly parallel (instead of executing a sequential instruction stream); functions executing in parallel do not affect each other's speed, so there can be greater throughput even at lower clock speeds. Latencies can be lower because each input and output can be connected directly to the FPGA (instead of connecting them all through a shared bus). Precision (word length) can be tailored to computational requirements (instead of relying on a few fixed word sizes).

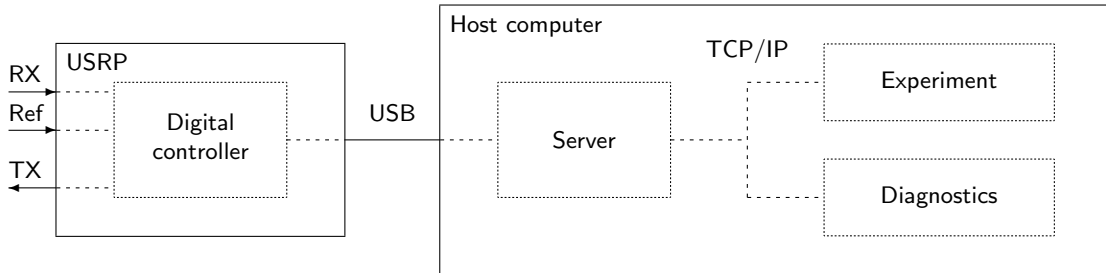


FIG. 2: System hardware and software

This controller accommodates input and output signals up to 2 volts peak-to-peak (-1V to +1V), digitized with a resolution of 12 bits (input) and 14 bits (output). The sampling frequency can be 64 MHz, or can be *decimated* (divided down) under software control. The controller demonstration described here samples at 500 kHz, chosen for acoustic cantilevers with resonant frequencies near 8 kHz. The controller includes an infinite impulse response (IIR) digital filter comprising two cascaded second-order sections (biquadratic sections, commonly called “biquads”). The signal and the filter coefficients are represented by 24-bit integers. The experiment software translates floating point to appropriately scaled 24-bit integers.

In addition to the filter, the controller also includes an input multiplexer and adder that selects and optionally adds two input signals in all combinations. This is helpful for some calibration protocols.

The controller characteristics (filter coefficients, multiplexer settings etc.) can be set and adjusted by control software while an experiment is running.

We expect that this controller will accommodate future microscopes in our laboratory with modest effort, and we believe it could be used elsewhere as well.

II. HARDWARE

Figure 2 shows the cantilever controller system, including the two main hardware components (solid boxes): the host computer and the USRP (Universal Software Radio Peripheral), which acts as the controller. The USRP and host communicate over a USB 2.0 (Universal Serial Bus). The USRP is in its own small case (21 cm wide, 5 cm high, 14 cm deep) and the bus runs through a cable (up to 5 m, longer with extensions), so it is easy to connect the USRP to a different host.

A. USRP (Controller)

All of the controller hardware including the FPGA, data converters, timing, signal conditioning, and connectors are included in the USRP [8, 9]. The USRP is designed to support software-defined radio, in particular the open-source GNU Radio project [10]. Its design is open source; its schematics are included in the GNU Radio software distribution. The USRP is commercially available.

Figure 3 shows the signal path through the USRP: the signal travels from left to right (horizontal solid lines), digitized control parameters from the host computer enter on the USB bus (vertical

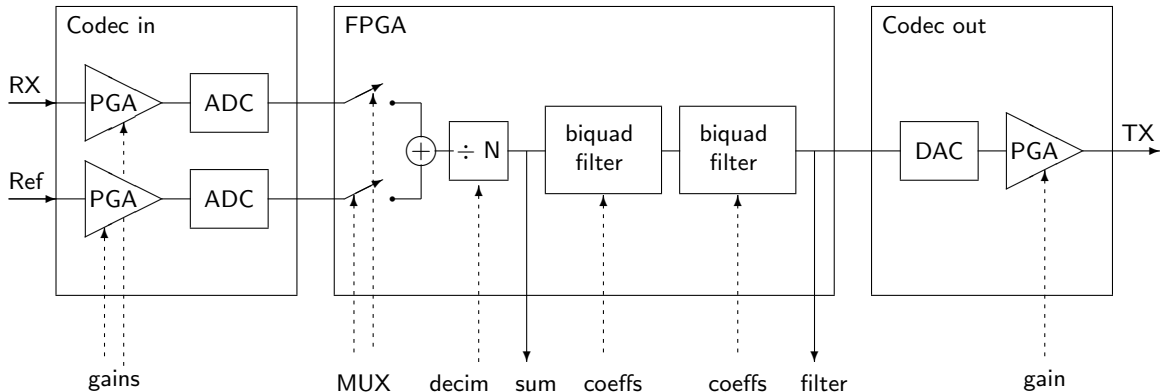


FIG. 3: Controller signal path

dotted lines) and the digitized acquired signals for the host computer exit on the USB (vertical solid lines). The multiplexer, decimator, and filters execute on the FPGA, an Altera Cyclone EP1C12, which provides 12,060 logic elements (each comprising several logic gates) and 239,616 bits of storage [11]. The data converters on the USRP are included in two Analog Devices AD9862 codecs, each with two analog to digital converters (ADC) and two digital to analog converters (DAC) [12]. The ADCs have 12 bit resolution; the DACs have 14 bit resolution. The AD9862 also includes programmable gain amplifiers (PGA) at the input of each ADC and the output of each DAC. The two blocks labelled “Codec in” and “Codec out” in Fig. 3 represent different parts of a single AD9862 device (there is one additional DAC with PGA which we do not use).

The ADC output pins are connected directly to FPGA input pins, so the digitized signal reaches the FPGA with less latency than would be possible if the ADCs were connected through a bus shared by several devices (as is common in microprocessors, including DSPs).

The ADCs sample at 64 MHz and the FPGA is clocked at 64 MHz. The DAC samples at 128 MHz. The FPGA program includes a decimator ($\div N$ in Fig. 3) which can divide down the sampling frequency used by the filters. The precision required for the filter coefficients increases as the sampling frequency grows relative to the resonant frequency of the filter. A programmable sampling frequency makes it possible implement filters that work well over a wide range of signal frequencies, even when the filter coefficients are represented with limited precision. A good compromise for a filter with resonance near 8 kHz divides the 64 MHz clock by 128 to sample at 500 kHz.

The FPGA, codecs, and USB hardware are on the USRP motherboard. The USRP also includes two daughterboards, LFRX and LFTX (Low-Frequency Receiver and Transmitter, where low frequency means below 30 MHz). These provide connectors and AD813x differential amplifiers at the inputs and outputs for buffering and signal conditioning [13]. The amplifier circuits are fixed at unity gain and 50 ohm impedance. The daughterboards have no programmable elements (daughterboard components do not appear in Fig. 3).

The signal path shown in Fig. 3 only uses half the USRP: one of two AD9862 codecs, and two of four daughterboards. Another independent signal path could be accommodated in the same USRP. Both signal paths would execute in parallel so both would run at full speed.

B. Host computer

The host computer stores the controller program that runs on the FPGA. Before an experiment, a program on the host computer loads the controller program into the FPGA. During an experi-

ment, the host computer executes experiment control software that can set and adjust controller parameters and acquire the measured signals.

III. SOFTWARE

A. Controller software

The controller program comprising the multiplexer and digital filter executes on the FPGA in the USRP.

The multiplexer selects among input signals to connect to the digital filter. It can connect the cantilever position signal or a reference signal (RX or Ref in Fig. 3), or neither, or their sum. All four combinations are used in our calibration protocols.

The filter consists of two second-order stages, also called *biquadratic* stages, commonly called “biquads”. Each stage implements a transfer function represented by a ratio of second-order polynomials, with three coefficients in both the numerator and denominator. The signals and coefficients are 24-bit integers. Using biquad stages requires less precision than a single higher-order filter.

Two biquad filter stages are sufficient to implement transfer functions for optimal cantilever controllers derived by the method of the appendix. The transfer functions are computed and then translated to biquad stages by software on the host computer (section III B).

In addition to the controller itself, the FPGA also executes code that communicates with the host computer over the USB. The bus control code, and several modules used by the controller, are from the open-source GNU Radio project [10].

The controller program is written in the Verilog hardware description language (HDL) [14]. The several Verilog source files are compiled or *synthesized* into a single binary file called a *bitstream* which is stored on the host computer and loaded into the FPGA on command. An FPGA can be reprogrammed by loading another bitstream. The host computer can store several bitstreams that provide different controller capabilities and load them into the FPGA under program control.

The *word length* is the number of bits used to represent numbers in a program. An FPGA program can specify any word length at each stage in each computation, unlike a conventional processor or DSP where only a small fixed set of word lengths is supported by the machine arithmetic. FPGA capacity is limited, so an important design task is to choose the minimum word lengths that provide sufficient accuracy. Different word lengths can be chosen for the signal path (solid lines in Fig. 3) and for the filter coefficients (dotted lines near the center of Fig. 3).

If the word length of the signal path is too small, the filter exhibits a nonlinear input/output relation with a threshold at small amplitudes and saturation at large amplitudes. With a 16-bit signal path, the linear range is only from about 0.1 V to 0.5 V input amplitude, which is too little dynamic range for our experiments. The word length required for the filter coefficients increases as the sampling frequency grows relative to the resonant frequency of the filter. If the word length of the coefficients is too small, the actual resonant frequency of the filter differs from the intended (computed) value. A good compromise for a filter with resonance near 8 kHz divides the 64 MHz clock by 128 to sample at 500 kHz. Under these conditions, 16 bit coefficients can result in an actual resonant frequency that differs about 16 Hz from the intended value, which is too much for our experiments. We found that 24 bits were adequate for both signal path and coefficients; some intermediate results use word lengths up to 50 bits. We found the acceptable word lengths by trial and error, although did do some simulations in MATLAB [15] to confirm that the symptoms we observed were explained by the limited word length, rather than programming errors or some other cause.

We have only very limited ability to observe and debug synthesized Verilog code executing on the FPGA. Therefore we do most debugging in simulation. First we check the design in MATLAB, as described above. Then on the host computer we write the Verilog code and use the Icarus Verilog compiler to build an executable simulation [16]. We execute the simulation on the host and use the GTKWave viewer on the host to show its results in a display that resembles an oscilloscope or logic analyzer [17]. Finally we use a synthesizer to compile the debugged Verilog to a bitstream that can be executed on the FPGA [18].

The bitstream for this controller program uses 2,765 logic elements and 66,304 memory bits in the FPGA, about one fourth of the available resources. Another independent signal path could be accommodated in the same FPGA, or higher-order transfer functions could be implemented by adding more biquad filter stages.

The controller software is open source and is available from the project web site [19].

The measured performance of the controller is discussed in section IV.

B. Host computer software

The experiment software including calibration protocols, data acquisition and storage, calculation of the controller transfer function, etc., executes on the host computer.

The host software is organized as a client and server. The client comprises most of the experiment control, while the server is a small component that copes with the details of the controller and its interface. For example, the client calculates the transfer function for the optimal cantilever controller as described in the appendix. The transfer function is represented as a ratio of polynomials with four numerator and four denominator coefficients. The server transforms this transfer function for two cascaded biquad sections by factoring the polynomials, sorting and collecting factors, then multiplying them in two groups. It also replaces floating point coefficients with scaled 24-bit integers. It loads the integer coefficients into particular registers in the FPGA using the USB. The client software does not depend on controller details such as filter architecture, hardware organization, number representation, and connection technology; these only affect the server. Therefore the same server could be used with different experiments; the particulars of each experiment are encoded in the client. Thanks to this organization, our client software is largely unchanged from earlier versions that used completely different controller technology based on a DSP.

Client and server communicate by sending text messages over a TCP/IP socket connection. In Fig. 3, both execute on the same computer. They can also execute on different computers (we have used both configurations).

The server also performs data acquisition, acquiring the stream of digitized samples from the FPGA at two points in the signal path: the outputs of the multiplexer and the digital filter (labeled “sum” and “filter” in Fig. 3). The server can optionally display these data as a spectrum or time series on an oscilloscope-like display, as shown in Fig. 4.

The server is written in Python and uses libraries from the open source GNU Radio and SciPy projects [10, 20, 21].

Our usual client is a large experiment control program written in LabView [22]. We also wrote a small client in Python for diagnostics and testing. Both clients can run at the same time, because both open and close the socket connection each time they send a message.

The host software is open source and is available from the project web site [19].

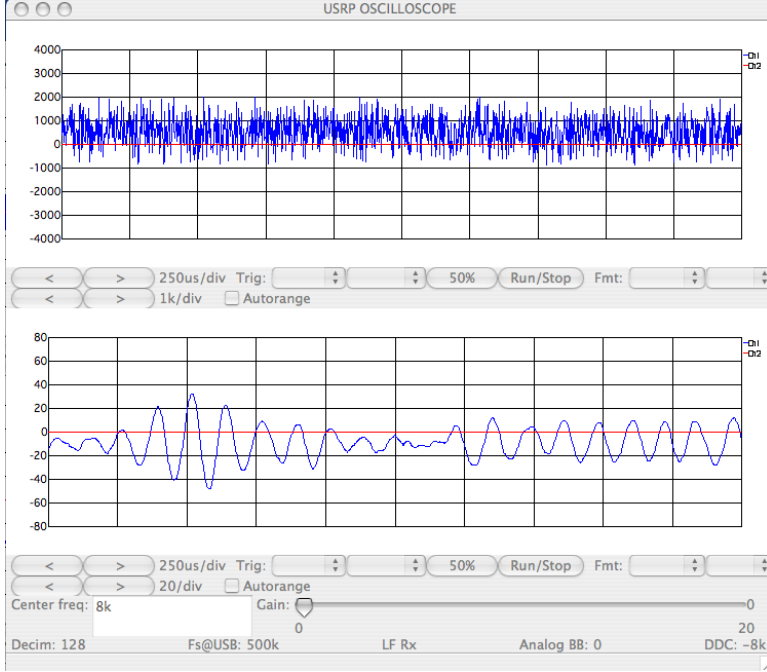


FIG. 4: Server program oscilloscope-like display

IV. PERFORMANCE

We compared a computed transfer function to the transfer function inferred from measurements of the analog signals at the input and output of the controller, and found close agreement (Figs. 5 and 6). For this test we used a controller transfer function that we had computed for a typical MRFM experiment, by the method of the appendix, where the cantilever had resonant frequency near 8000 Hz and an uncontrolled resonant quality Q near 10,000. The transfer function is described by the four b (numerator) and four a (denominator) coefficients in table I.

b_i	$7.026189 \cdot 10^{-5}$	$1.027999 \cdot 10^{-4}$	$-5.927540 \cdot 10^{-5}$	$-9.181339 \cdot 10^{-5}$
a_i	$1.000000 \cdot 10^0$	$-2.848528 \cdot 10^0$	$2.708790 \cdot 10^0$	$-8.588522 \cdot 10^{-1}$

TABLE I: Controller transfer function (index i ranges from 0 to 3, left to right)

Plots of the computed transfer function appear as solid lines in Figs. 5 (amplitude) and 6 (phase). At the resonant frequency, the ratio of the output amplitude to the input amplitude is about 1.4, and the output phase lags the input phase by about 80 degrees. The server software factors and scales this transfer function into two cascaded biquad sections with 24-bit integer coefficients (table II).

	Section 0			Section 1		
b_i	35158	2293	-32865	35158	-49146	0
a_i	-4194304	8339278	-4187298	-4194304	3608314	0

TABLE II: Controller filter coefficients (in each section index i ranges from 0 to 2, left to right)

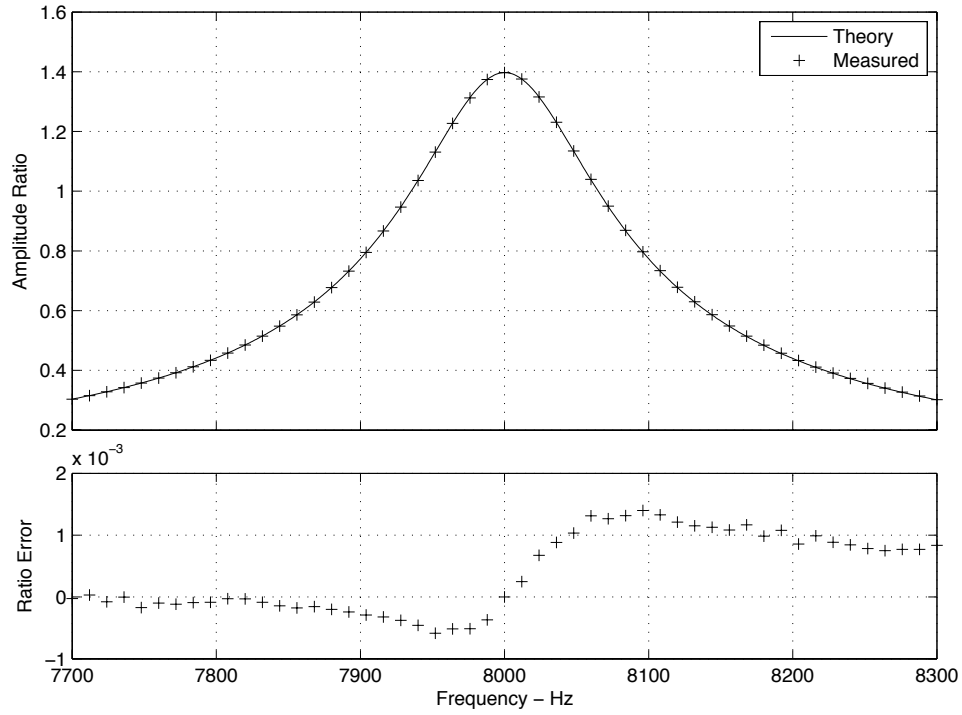


FIG. 5: Calculated and measured transfer functions: amplitude

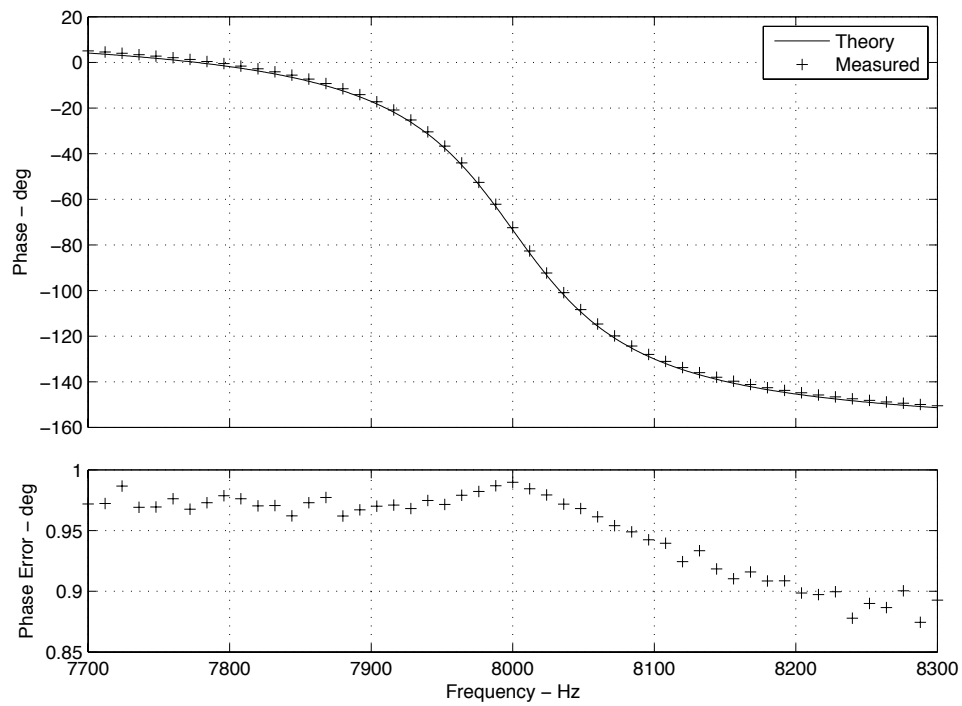


FIG. 6: Calculated and measured transfer functions: phase

We measured the controller transfer function with a lock-in amplifier [23]. The SINE OUT signal from the lock-in was applied to the input to the controller (RX in figs. 2 and 3). The experiment software commanded the lock-in amplifier to generate sine waves from 7700 to 8300 Hz at 100 Hz intervals. The sine wave amplitude was adjusted to 0.100 V. The output from the controller (TX in the figures) was applied to the SIGNAL IN A-I input of the lock-in. At each frequency, the in-phase and quadrature components X and Y of the controller output were calculated by the lock-in amplifier, with a time constant of 3 sec, and the experiment software calculated the amplitude and phase of the transfer function from X and Y samples. The measured transfer function points appear as crosses in Figs. 5 (amplitude) and 6 (phase). The errors (differences between calculated and measured values) appear in the plots below the transfer functions. The amplitude ratio error is less than 0.002, and the phase error is less than one degree, over the entire measured frequency range. These errors are acceptable in our experiment.

The computed and measured transfer functions have a phase lag of about 80 degrees at the resonant frequency. The computed transfer function includes phase compensation to account for the phase lag contributed by various components in the entire signal path (appendix, Fig. 9 and section 3 e). The lag contributed by the fixed latency of the digital controller was estimated by applying a 50 Hz square wave to the input and observing (on an oscilloscope) the delay until the output starts ringing. This showed a latency of about 2 usec, similar to the sampling interval (at the 500 kHz sampling frequency), so the digital controller contributes about 6 degrees of lag at 8000 Hz.

The gains of the PGAs (Fig. 3) were set to to 1, nominally. This results in (nearly) equal amplitudes for RX and TX, when a controller with unity gain is loaded. The PGAs are not precisely calibrated so the overall gain is not exactly 1.0. It is possible to trim the output PGA (via software) to obtain an overall gain very near 1.0, but we choose instead to simply keep track of the observed overall gain in our experiment software. The observed overall gain in these measurements was 1.038.

V. APPLICATION

We used the controller in an experiment with a cantilever with a resonant frequency of 8347 Hz and an uncontrolled Q of about 10,000. Figure 7 shows the one-sided power spectrum of the noise measured (by a spectrum analyzer [24]) from the controlled cantilever with several different controller transfer functions, with controlled Q values 75, 100, 200, 300 and 400. These measurements show the expected results.

VI. DISCUSSION

We anticipate adapting the platform described here to different control schemes. The following paragraphs describe one that we are considering.

A goal of MRFM is to achieve atomic-scale resolution by resolving individual nuclear spins. A promising approach to this goal would use cantilevers that oscillate at radio frequencies (1 – 10 MHz) [25]. Such high cantilever frequencies press the performance limits of available digital control technologies. An alternative uses *heterodyne control*, where the central controller elements process signals at much lower frequencies than the cantilever oscillation [26]. It confers another potential advantage because a heterodyne controller might also act as the lock-in detector for the MRFM signal, eliminating the separate lock-in amplifier we now use in our experiments [7].

In earlier work, we demonstrated a digital heterodyne controller with an emulated radio frequency cantilever [26] (our emulation was a real-time digital simulation with analog inputs and

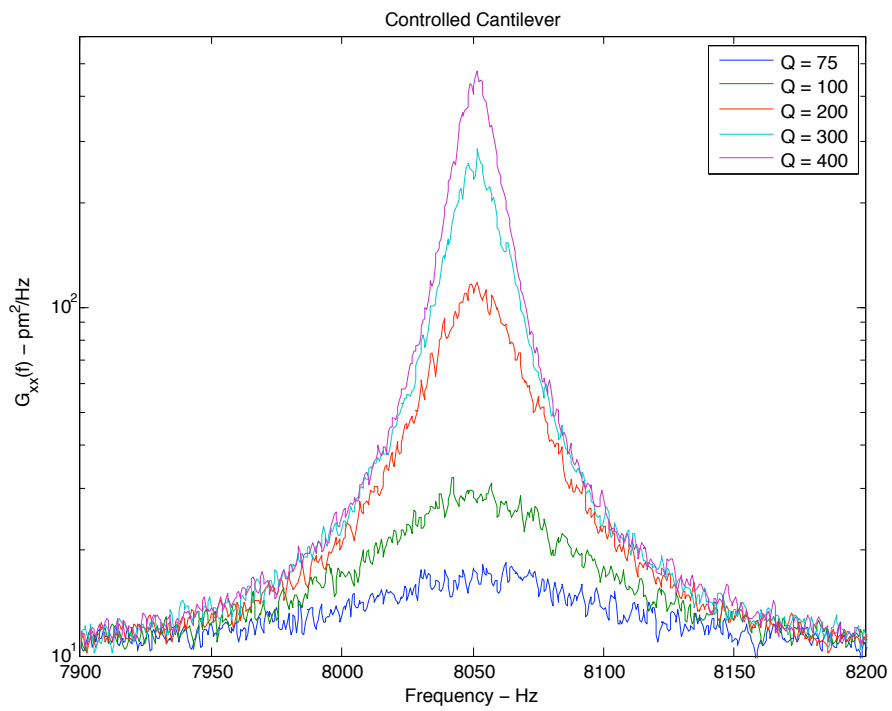


FIG. 7: Controlled cantilever power spectra

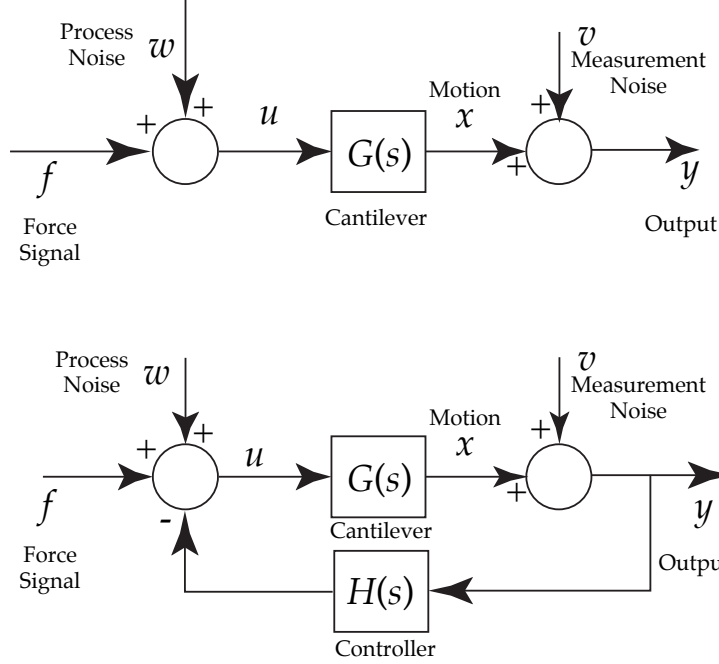


FIG. 8: Open and closed loop dynamic systems

outputs that resembled the signals expected from a radio frequency cantilever). We have begun experimenting with an FPGA implementation of a heterodyne controller [27]. The hardware and host computer software is the same as described here. The only difference is the FPGA code for the controller, which implements a different block diagram than the one shown here in Fig. 3.

Acknowledgments

This work was supported by the Army Research Office (ARO) Multi-University Research Initiative (MURI) W911NF-05-1-0403.

APPENDIX: CONTROLLER TRANSFER FUNCTION

Here we show how to calculate filter coefficients for an optimal controller from measured cantilever characteristics. We derive the controller transfer function, following the theory of optimal feedback control of force cantilevers in [3]. After reviewing briefly the continuous-time specification of that controller, we derive a discrete-time equivalent. Practical hardware and software issues, along with compensation of parasitic effects, are treated.

1. Continuous-time Control

In Fig. 8, a linear dynamic feedback control element is added to the open loop system. The dynamic relationship between the forces u applied to the cantilever tip and the motion x of the tip is represented by the transfer function $G(s)$. In addition, f is the force signal to be detected, w is additive process noise force, v is measurement noise added to the actual position of the cantilever, and $H(s)$ is the transfer function of the feedback controller.

Many techniques are available for the design of $H(s)$. All require knowledge of the physical characteristics of the cantilever, the noise processes w and v , and a design goal for controller performance. Below, the techniques of optimal control and estimation are combined to determine the continuous-time transfer function of the controller $H_{oc}(s)$ which relates measured motion of the cantilever y to the control component of the input force u (Eq. (31) of [3]).

$$H_{oc}(s) = \frac{U(s)}{Y(s)} = \frac{K_{oc}(s + z_{oc})}{s^2 + \frac{\omega_{oc}}{Q_{oc}}s + \omega_{oc}^2}, \quad (\text{A.1})$$

where

$$\frac{K_{oc}}{\omega_n} = \frac{1}{2}k\alpha\beta(\alpha + \beta) + \frac{k\alpha\beta}{Q},$$

$$\frac{z_{oc}}{\omega_n} = \frac{\frac{\alpha\beta}{2} - 2 + \frac{\alpha+\beta}{Q} + \frac{2}{Q^2}}{\alpha + \beta + \frac{2}{Q}},$$

$$\frac{\omega_{oc}^2}{\omega_n^2} = \frac{(\alpha + \beta)^2}{2} + \frac{\alpha + \beta}{Q} + 1,$$

$$Q_{oc} = \frac{\sqrt{\frac{(\alpha+\beta)^2}{2} + \frac{\alpha+\beta}{Q} + 1}}{\alpha + \beta + \frac{1}{Q}}.$$

where k , ω_n , and Q are the stiffness, natural frequency, and resonant quality of a single-mode cantilever model. The parameters α and β are determined from the control and estimation requirements.

The value of α is defined by the need to keep the system stationary within acceptable deviations from $x = 0$, while using acceptable amounts of control u .

$$\alpha = \sqrt{\frac{1}{Q^2} + 2\xi^2} - \frac{1}{Q} \text{ and } \xi^2 = \sqrt{1 + \frac{U}{k^2X}} - 1. \quad (\text{A.2})$$

α is a function of the maximum allowed variances of the displacement $X = E[x_m^2]_{max}$ and the control force $U = E[u^2]_{max}$. The definitions of ξ and α indicate that the relevant physical parameter is the ratio of the maximum control force to the force that would be caused in a spring subjected to the maximum displacement.

The estimator parameter β represents the quality of the data used to estimate the system state, and is determined by the relative amounts of process and measurement noise.

$$\beta = \sqrt{\frac{1}{Q^2} + 2\psi^2} - \frac{1}{Q} \text{ and } \psi^2 = \sqrt{1 + \frac{W}{k^2V}} - 1. \quad (\text{A.3})$$

where constants W and V are the power spectral densities of stationary, zero-mean, Gauss-Markov random processes. Large measurement noise means that the observations are weighted less in the estimate of the state, while small measurement noise allows large gains in the estimator.

The controller has two complex poles and a real zero. As the allowable control effort is increased (greater α), or the measurement noise is reduced (greater β), the natural frequency of the controller rises and its Q_{oc} is diminished. Again, in the limit as $(\alpha + \beta)$ approaches infinity, Q_{oc} approaches $\sqrt{2}/2$.

Ultimately, the control accuracy can be no better than the inferred state. The control value, $\langle u^2 \rangle$, approaches infinity as $\alpha \rightarrow \infty$. However, even when large control effort is available, little is gained by allowing α to be arbitrarily large. The poles of the closed loop system are the union of the poles of the optimal controller and estimator. Since poles of smaller magnitude will tend to dominate the dynamic response, a practical guide is to make α smaller than β , but of similar magnitude.

While the closed-loop system is of fourth order, it is often useful to describe the controller design goal in terms of the effective resonant quality Q_{cl} of the dominant closed-loop poles. Assuming that α is smaller than β , the value of α corresponding to the closed-loop quality Q_{cl} is given by (Eq. (16) of [3])

$$\alpha = \frac{1}{Q} \left[1 - \sqrt{\frac{2Q^2 - 1}{2Q_{cl}^2 - 1}} \right] \simeq \frac{1}{Q_{cl}} - \frac{1}{Q}. \quad (\text{A.4})$$

Alternately the design goal can be stated in terms of the closely related quantities: the bandwidth $\Delta\omega_{cl} = \omega_n/Q_{cl}$, or the damping time $\tau_{cl} = 2Q_{cl}/\omega_n$.

Finally, the performance of the optimally controlled closed loop system in terms of the mean-square cantilever displacement and control force can be predicted from (Eqs. 38-39 of [3])

$$\frac{\langle x_m^2 \rangle}{\omega_n} = \frac{V\beta \left[\frac{2\alpha^2 + \beta^2}{2} + \frac{2\alpha + \beta}{Q} + \alpha\beta + 2 \right] \left[\frac{2\alpha + \beta}{2} + \frac{1}{Q} \right]}{\left[\alpha + \frac{1}{Q} \right] \left[\alpha^2 + \frac{2\alpha}{Q} + 2 \right]}, \quad (\text{A.5})$$

and (Eq. (39) of [3])

$$\begin{aligned} \frac{\langle u^2 \rangle}{\omega_n} = & \frac{V(k\alpha\beta)^2}{8\left(\alpha + \frac{1}{Q}\right)\left(\alpha^2 + \frac{2\alpha}{Q} + 2\right)} \times \\ & \left[\alpha^4 + 2\alpha^3\beta + 2\alpha^2 + 2\beta^2 + \frac{3}{2}\alpha^2\beta^2 + 8 + \right. \\ & \frac{6\alpha^3 + 10\beta\alpha^2 + 4\beta^2\alpha}{Q} + \frac{2\beta^2 - 8 + 14\alpha^2 + 16\alpha\beta}{Q^2} + \\ & \left. \frac{8\alpha + 16\beta}{Q^3} + \frac{8}{Q^4} \right]. \quad (\text{A.6}) \end{aligned}$$

Since β is a function of V , it is useful to express V in Eqs. (A.5) and (A.6) in terms of the (experimentally measured) *uncontrolled* (open loop) rms amplitude $\langle y_{ol}^2 \rangle^{\frac{1}{2}}$

$$V = \frac{8\langle y_{ol}^2 \rangle^{\frac{1}{2}} Q / \omega_n}{(\beta^4 + 4\beta^2)Q^2 + 4\left(4\frac{\Delta\omega_V}{\pi\omega_n} + 2\beta + \beta^3\right)Q + 4\beta^2} \quad (\text{A.7})$$

where $\Delta\omega_V$ is the effective measurement noise bandwidth.

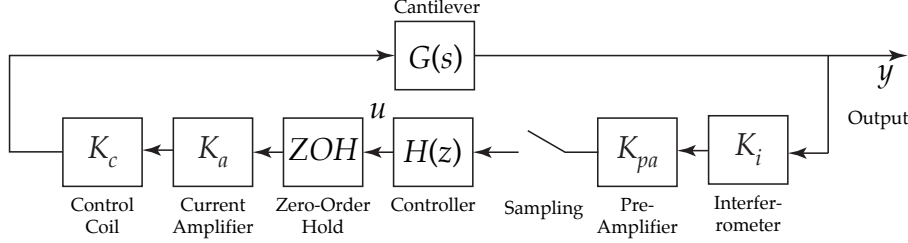


FIG. 9: Implementation block diagram

2. Discrete-time Control

The digital controller shown in Fig. 3 implements the feedback element $H(s)$. The digital controller periodically samples the voltage signal corresponding to the measured cantilever motion, computes the appropriate control law, and imposes the result through a zero-order hold at its output. In our case, the control law is a discrete-time equivalent of the continuous-time transfer function in Eq. (A.1).

In general, the control law implemented by the digital controller can be any linear causal time-invariant difference equation of the form

$$y(n) = - \sum_{k=1}^N \frac{a_k}{a_0} y(n-k) + \sum_{k=0}^M \frac{b_k}{a_0} x(n-k) \quad (\text{A.8})$$

where $y(n)$ and $x(n)$ are samples of the output and input respectively, and a_k and b_k are constants.

Before we derive the difference equation several hardware and software issues must be considered.

3. Implementation Considerations

Figure 9 shows the complete cantilever control system, including the elements of cantilever motion sensing, force actuation, conversion and amplification. Below, we consider the specifications and characteristics of each block. Throughout, we assume that the A/D and D/A converters are linear with inversely related gains: $K_{ad} = 1/K_{da}$.

a. Sampling Rate

Faithful discrete-time reproduction of the continuous-time controller requires that the sampling rate be large in comparison with the natural frequency of the system. A good rule-of-thumb is to select a sampling frequency at least 30 times larger than the cantilever natural frequency. Typically, our sampling rate is 0.5 MHz for a natural frequency of 7500 Hz.

b. The interferometer

The fiber optic interferometer converts the displacement of the cantilever into a proportional voltage signal. A typical sensitivity for our interferometer is $K_i = 10 \times 10^6$ V/m. The interferom-

eter bandwidth is limited to approximately 100 kHz.

c. Force Actuator

Magnetic actuation provides the restoring feedback force to the cantilever. The force is proportional to the current passing through the control coil. The actuator can be calibrated by driving the coil (open loop) with a sinusoidal current of known amplitude at the cantilever natural frequency, and measuring the resulting cantilever motion. From that measurement and the known stiffness, quality, and natural frequency of the cantilever, the actuator sensitivity K_c is determined.

A typical actuator gain is $K_c = 35 \times 10^{-12}$ N/A.

d. Amplification

Two stages of amplification are used to match the dynamic ranges of the interferometer and coil actuator to the input/output ranges of the digital controller.

Suppose that the full-scale ranges of both the A/D and D/A converters are V_{fs} . A simple strategy is to select the interferometer pre-amplifier gain K_{pa} such that the predicted rms value of the controller input is one third of the A/D converter range:

$$K_{pa} = \frac{V_{fs}}{3K_i\sqrt{\langle x_m^2 \rangle + \frac{\Delta\omega_n V}{\pi}}} \tag{A.9}$$

Then select the current amplifier gain K_a such that the predicted rms value of the controller output is one third of the D/A converter range:

$$K_a = \frac{3\langle u^2 \rangle^{\frac{1}{2}}}{K_c V_{fs}} \tag{A.10}$$

These rules ensure that signals substantially fill the A/D and D/A converter ranges (thereby minimizing quantization noise), while only rarely allowing the signals to exceed those ranges.

For our system, the converter ranges are $V_{fs} = 1$ V. Typical gain values are $K_{pa} = 14.4$ V/V, and $K_a = 0.001$ A/V.

e. Phase-lead Compensation

The optimal controller described in Eq. (A.1) was derived under the assumption that the remainder of the control loop in Fig. 8 consists only of the single-mode (2nd order) cantilever model. As we have seen, any practical implementation includes additional dynamic components. The primary effect of these components is to introduce additional phase lag within the relatively narrow bandwidth of the controlled cantilever. Generally, phase lag tends to lower the damping, causing the performance to deviate from the predictions of Eqs. (A.5) and (A.6).

Sources of additional phase lag include:

- Finite bandwidths of the interferometer, its pre-amplifier, and the actuator coil current amplifier. Each device is characterized by low gain and large phase lag at high frequencies. Even components with bandwidths exceeding 0.1 MHz, will each contribute a few degrees of phase lag at the cantilever frequency.
- The A/D conversion delay T_d causes an effective phase lag of ωT_d radians.
- Similarly, the D/A converter zero-order hold, of sample time T , adds $\omega T/2$ radians of phase lag.

While analytical predictions are useful, the most reliable method of determining the *total* phase lag is by careful measurement of the actual system. Minor phase lag will not seriously alter the system behavior and, in many cases, can be ignored. Of course, we could have accounted for the transfer function of each of these additional components during the design of the controller. However, a closed-form solution for the controller would not be possible, and the insight afforded by Eq. (A.1) would be lost. Instead, we can easily compensate for the phase lag by augmenting the control law with a phase-lead dynamic component.

Consider the following simple phase-lead transfer function

$$G_c(s) = \frac{(1 + \eta\tau s)}{\sqrt{\eta}(1 + \tau s)} \tag{A.11}$$

where

$$\eta = \frac{1 + \sin \phi_m}{1 - \sin \phi_m} \quad \text{and} \quad \tau = \frac{1}{\omega_m \sqrt{\eta}}$$

As shown in Fig. 10, at the center frequency ω_m the magnitude of the transfer function is unity, and the phase angle is ϕ_m . By assigning ω_m to the controller natural frequency, and concatenating this compensator with the controller definition in Eq. (A.1) phase lags of up to 60 degrees can be corrected.

f. Tustin's Approximation

Having considered all of the components in the control loop, we derive a practical discrete-time equivalent of the control law (A.1). A variety of transformation methods can be used: numerical integration, zero-pole matching, hold equivalents, etc. Here we will use a trapezoidal numerical integration technique, known in control circles as Tustin's method or the bilinear transformation.

Given a continuous-time transfer function $H(s)$, the z -transform of a Tustin discrete equivalent can be found by substitution

$$H(z) = H(s) \Big|_{s = \frac{2}{T} \frac{z-1}{z+1}} \tag{A.12}$$

where T is the sampling interval.

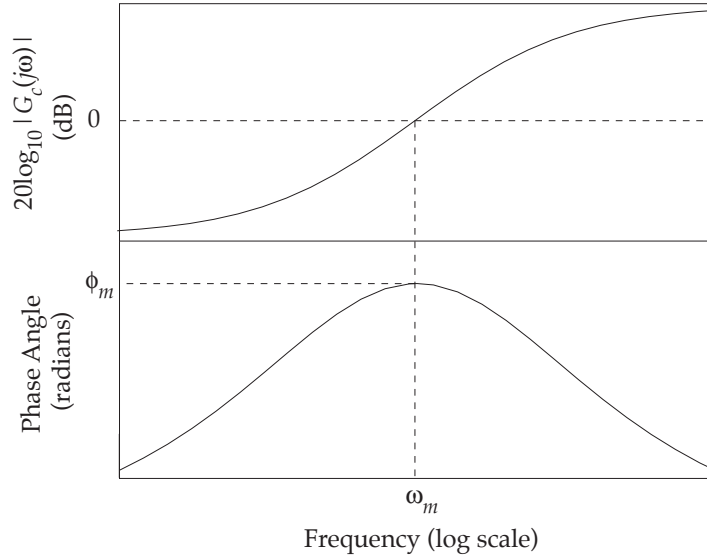


FIG. 10: Phase-lead compensation Bode diagram

The resulting discrete transfer function $H(z)$ is the ratio of two polynomials in z and is of the form

$$H(z) = \frac{\sum_{k=0}^M b_k z^{-k}}{\sum_{k=0}^N a_k z^{-k}} \quad (\text{A.13})$$

For purposes of controller computation, the constants a_k and b_k are arranged into the corresponding difference equation of the form shown in (A.8).

g. Prewarping

The bilinear transformation maps the stable region of the s -plane (the left half plane) exactly into the finite region within the unit circle of the z -plane. Clearly, distortion takes place in this mapping, such that the frequency responses of $H(s)$ and $H(z)$ differ. We can force the discrete equivalent to match $H(s)$ at the controller natural frequency by “prewarping” the continuous-time transfer function. Expressing $H(s)$ as $H(\frac{s}{\omega_{oc}})$, replace ω_{oc} with ω_a such that

$$\omega_a = \frac{2}{T} \tan \frac{\omega_{oc} T}{2} \quad (\text{A.14})$$

Notice that ω_a approaches ω_{oc} for high sampling rates. Stated as a frequency substitution the prewarped Tustin equivalent is described as

$$H(z) = H\left(\frac{s}{\omega_{oc}}\right) \Bigg|_{\frac{s}{\omega_{oc}} = \frac{1}{\tan(\omega_{oc} T/2)} \frac{z-1}{z+1}} \quad (\text{A.15})$$

4. The Complete Controller

Finally, the complete discrete-time controller can be assembled. To maintain the loop gain $G(s)H(s)$ in Fig. 8, we must adjust the original control law (A.1) to account for the additional gain elements in Fig. 9. Combining the optimal controller with the phase-lead compensator we have the continuous-time control element.

$$H(s)G_c(s) = \frac{K_{oc}}{K_a K_{pa} K_c K_i \sqrt{\eta}} \times \frac{(s + z_{oc})(1 + \eta\tau s)}{(s^2 + (\omega_{oc}/Q_{oc})s + \omega_{oc}^2)(1 + \tau s)} \quad (\text{A.16})$$

The coefficients of the corresponding difference equation (A.8) are derived using the prewarped Tustin's approximation (A.15)

$$\begin{aligned} a_0 &= 1 \\ a_1 &= \frac{(-\omega' - 3\tau' + 3\omega'^3 + \omega'^2\tau')Q_{oc} + \omega'^2 - \omega'\tau'}{(\omega'^3 + \omega'^2\tau' + \omega' + \tau')Q_{oc} + \omega'^2 + \omega'\tau'} \\ a_2 &= \frac{(-\omega' + 3\tau' + 3\omega'^3 - \omega'^2\tau')Q_{oc} - \omega'^2 - \omega'\tau'}{(\omega'^3 + \omega'^2\tau' + \omega' + \tau')Q_{oc} + \omega'^2 + \omega'\tau'} \\ a_3 &= \frac{(\omega' - \tau' + \omega'^3 - \omega'^2\tau')Q_{oc} - \omega'^2 + \omega'\tau'}{(\omega'^3 + \omega'^2\tau' + \omega' + \tau')Q_{oc} + \omega'^2 + \omega'\tau'} \end{aligned} \quad (\text{A.17})$$

and

$$\begin{aligned} b_0 &= \frac{Q_{oc}\omega'K'}{K_a K_{pa} K_c K_i \sqrt{\eta}} \times \frac{\omega' + \eta\tau' + \omega'\eta z'_{oc}\tau' + \omega'^2 z'_{oc}}{(\omega'^3 + \omega'^2\tau' + \omega' + \tau')Q_{oc} + \omega'^2 + \omega'\tau'} \\ b_1 &= b_0 \frac{\omega' - \eta\tau' + \omega'\eta z'_{oc}\tau' + 3\omega'^2 z'_{oc}}{\omega' + \eta\tau' + \omega'\eta z'_{oc}\tau' + \omega'^2 z'_{oc}} \\ b_2 &= -b_0 \frac{\omega' + \eta\tau' + \omega'\eta z'_{oc}\tau' - 3\omega'^2 z'_{oc}}{\omega' + \eta\tau' + \omega'\eta z'_{oc}\tau' + \omega'^2 z'_{oc}} \\ b_3 &= -b_0 \frac{\omega' - \eta\tau' + \omega'\eta z'_{oc}\tau' - \omega'^2 z'_{oc}}{\omega' + \eta\tau' + \omega'\eta z'_{oc}\tau' + \omega'^2 z'_{oc}} \end{aligned} \quad (\text{A.18})$$

where the normalized parameters are:

$$K' = \frac{K_{oc}}{\omega_{oc}}, \quad \tau' = \frac{1}{\sqrt{\eta}}, \quad z'_{oc} = \frac{z_{oc}}{\omega_{oc}}, \quad \text{and} \quad \omega' = \tan \frac{\omega_{oc}T}{2}.$$

A final note: Occasionally the controller output $y(n)$, calculated from the difference equation, will exceed the D/A converter range $[0, C_{da}]$. Since some converters wrap overranged values to the opposite edge of the range, it is essential that the output value be limited:

$$y(n)_{out} = \max(\min(y(n), C_{da}), 0) \quad (\text{A.19})$$

[1] J. A. Sidles, Applied Physics Letters **58**, 2854 (1991).

[2] J. A. Sidles, J. L. Garbini, K. J. Bruland, D. Rugar, O. Züger, S. Hoen, and C. S. Yannoni, Reviews of Modern Physics **67**, 249 (1995).

- [3] J. L. Garbini, K. J. Bruland, W. M. Dougherty, and J. A. Sidles, *Journal of Applied Physics* **80**, 1951 (1996).
- [4] K. J. Bruland, J. L. Garbini, W. M. Dougherty, and J. A. Sidles, *Journal of Applied Physics* **80**, 1959 (1996).
- [5] K. J. Bruland, J. L. Garbini, W. M. Dougherty, and J. A. Sidles, *Journal of Applied Physics* **83**, 3972 (1998).
- [6] C. L. Degen, U. Meier, Q. Lin, A. Hunkeler, and B. H. Meier, *Review of Scientific Instruments* **77** (2006).
- [7] S.-H. Chao, W. M. Dougherty, J. L. Garbini, and J. A. Sidles, *Review of Scientific Instruments* **75**, 1175 (2004).
- [8] Ettus Research LLC, *Universal Software Radio Peripheral (USRP)*, Mountain View, CA (2006), with LFRX and LFTX daughter boards.
- [9] GNU Radio project, USRP documents, URL <http://gnuradio.org/trac/wiki/USRP>.
- [10] GNU Radio project, software and instructions, URL <http://gnuradio.org/trac>.
- [11] Altera Corporation, *Cyclone FPGA Family Data Sheet*, San Jose, CA (2007).
- [12] Analog Devices, Inc., *AD9860/AD9862 Mixed-Signal Front-End (MxFE) Processor for Broadband Communications*, Norwood, MA (2002).
- [13] Analog Devices, Inc., *Using the AD813x*, Norwood, MA (2002), application note AN-584.
- [14] J. Bhasker, *Verilog HDL Synthesis: A Practical Primer* (Star Galaxy Publishers, Allentown, PA, 1998).
- [15] Mathworks, Inc., MATLAB software with Filter Design Toolbox and Fixed-Point Toolbox.
- [16] Icarus software, Verilog compiler and simulator, URL <http://www.icarus.com/eda/verilog/>.
- [17] GTKWave software, viewer, URL <http://home.nc.rr.com/gtkwave/>.
- [18] Altera Corporation, *Introduction to the Quartus II Software*, San Jose, CA (2007), ver 7.1.
- [19] J. Jacky, *MRFM cantilever control using FPGA*, software and instructions, URL <http://staff.washington.edu/jon/gr-mrfm>.
- [20] T. E. Oliphant, *Computing in Science and Engineering* pp. 10 – 20 (2007).
- [21] SciPy software, URL <http://www.scipy.org/SciPy>.
- [22] National Instruments, Inc., LabView software.
- [23] Stanford Research Systems, Inc., *SR850 DSP Lock-In Amplifier*, Sunnyvale, CA (1993).
- [24] Stanford Research Systems, Inc., *Model SR780 Network Signal Analyzer*, Sunnyvale, CA (1995).
- [25] J. A. Sidles, J. L. Garbini, and G. P. Drobny, *Review of Scientific Instruments* **63**, 3881 (1992).
- [26] T. E. Kriewall, J. L. Garbini, J. A. Sidles, and J. P. Jacky, *ASME Journal of Dynamic Systems, Measurement, and Control* **128**, 577 (2006).
- [27] GNU Radio project, FPGA code for heterodyne controller, URL <http://gnuradio.org/trac/browser/gnuradio/trunk/usrp/fpga/toplevel/mrfm>.